# *Ab initio* calculation of the electronic structure and spectroscopic properties of spinel $\gamma$-$Sn_3N_4$

W. Y. Ching and Paul Rulis
*Department of Physics, University of Missouri-Kansas City, Kansas City, Missouri 64110, USA*
(Received 26 August 2005; revised manuscript received 16 November 2005; published 5 January 2006)

The electronic structure and physical properties of $\gamma$-$Sn_3N_4$ in the spinel structure are investigated by first-principles calculations. The calculated band structure, electronic bonding, and optical properties are compared with two well-studied spinel nitrides $\gamma$-$Si_3N_4$ and $\gamma$-$Ge_3N_4$. $\gamma$-$Sn_3N_4$ is a semiconductor with a direct band gap of 1.40 eV and an attractive small electron effective mass of 0.17. Its optical properties are different from that of $\gamma$-$Si_3N_4$ and $\gamma$-$Ge_3N_4$ because of the difference in the conduction band minimum. The Sn $K$, Sn $L_3$, Sn $M_5$, and N $K$ edges of the x-ray-absorption near-edge structure spectra in $\gamma$-$Sn_3N_4$ are calculated using a supercell approach and are found to be rich in structures. These spectra are discussed in the context of the electronic structure of the unoccupied conduction band in the presence of the electron core-hole interaction. These calculated spectra can be used for the characterization of this novel compound.

DOI: 10.1103/PhysRevB.73.045202 PACS number(s): 71.20.Ps, 61.10.Ht, 78.20.Ci

## I. INTRODUCTION

The existence of the third phase of silicon nitride $\gamma$-$Si_3N_4$ in addition to the well-known hexagonal $\alpha$- and $\beta$-$Si_3N_4$ was first reported in 1999.[1] Sixfold bonding for Si is a rare occurrence in crystal chemistry, but for $\gamma$-$Si_3N_4$, Si occupies both the tetrahedral and octahedral sites of the cubic spinel lattice. The discovery of $\gamma$-$Si_3N_4$ at high temperature and pressure has stimulated much theoretical[2–17] and experimental investigation[18–30] of spinel nitrides as a new family of superhard materials. So far, only the binary compounds $\gamma$-$Si_3N_4$, $\gamma$-$Ge_3N_4$, and $\gamma$-$Sn_3N_4$ have been synthesized with experimentally measured properties reported. For the ternary compound involving both Si and Ge, there have been some controversies as to whether the synthesized material is a spinel solid solution of the form $\gamma$-$(Si_xGe_{1-x})_3N_4$ (Refs. 12, 24, and 29) or there actually exist single-phase crystals with well-defined occupation of either Si or Ge at the tetrahedral or octahedral sites.[5,11,12] On the theoretical and computational side, $\gamma$-$Si_3N_4$ and $\gamma$-$Ge_3N_4$ have been extensively studied by many groups.[2,4–10,13,14,17] In particular, Fang and co-workers have calculated the phonon spectrum and the thermodynamic properties of $\gamma$-$Si_3N_4$.[14] However, the $\gamma$-$Sn_3N_4$ phase has been mostly ignored.[31,32] We have published some preliminary electronic structure calculations and bulk properties of $\gamma$-$Sn_3N_4$ using the orthogonalized linear combination of the atomic orbitals (OLCAO) method as part of a systematic study of the structures and properties of all possible binary and ternary spinel nitrides from group-IVB and group-IVA elements.[8,11] In fact, a detailed study of $\gamma$-$Sn_3N_4$ is very important because it can reveal trends in group-IVB spinel nitrides where the increasing ionic size of the cation is concomitant with variation in the electronic structure. Unlike $\gamma$-$Si_3N_4$ and $\gamma$-$Ge_3N_4$ which are synthesized in a high-pressure and high-temperature environment using either a laser-heated diamond anvil cell or by shock-wave compression, $\gamma$-$Sn_3N_4$ can be synthesized by a rapid solid metathesim reaction[31] or from an annealed tin amid-imide precursor at ambient pressure.[33] Since the pressure and temperature requirements for $\gamma$-$Sn_3N_4$ are generally more modest, it should be easier to prepare samples in larger quantities.

In this paper, we present the results of detailed calculations of the electronic structure, bonding, and spectroscopic properties of $\gamma$-$Sn_3N_4$. In order to compare the results from the OLCAO calculation, we used the VASP (Vienna *ab-initio* simulation package) code[35–37] to optimize the cell parameters of $\gamma$-$Sn_3N_4$. Our motivation of using two well-tested methods with entirely different computational strategies is to check if there would be any significant disparities in the geometry and bulk properties. The VASP-relaxed crystal structure is then used in the calculations of the electronic structure, bonding, and optical properties using the OLCAO method. The calculated physical properties are then compared with those of $\gamma$-$Si_3N_4$ and $\gamma$-$Ge_3N_4$ using the same method. In particular, the x-ray-absorption near-edge structures (XANESs) or, similarly, the electron-energy-loss near-edge structures (ELNESs) of $\gamma$-$Sn_3N_4$ were calculated using a supercell method that takes into account the electron core-hole interaction.[34] So far, this more rigorous approach of calculating the XANES and ELNES spectra has only been implemented in the OLCAO method. The calculated spectra are the Sn $K$, Sn $L_3$, Sn $M_5$, and N $K$ edges which can be very useful for the characterization of synthesized samples. The calculation of optical properties of $\gamma$-$Sn_3N_4$ can be used to assess the potential for applications of $\gamma$-$Sn_3N_4$ in semiconductor technology. In conjunction with previous studies on $\gamma$-$Si_3N_4$ (Refs. 2 and 7) and $\gamma$-$Ge_3N_4$ (Ref. 7), a full understanding of the fundamental properties of $\gamma$-$Sn_3N_4$ can be achieved. In the next section the methods of our calculations are briefly outlined. In Sec. III, we present and discuss the results on the electronic structure, bonding, bulk, and spectroscopic properties of $\gamma$-$Sn_3N_4$. The last section is for a brief summary and some conclusions.

## II. METHOD OF CALCULATION

Several groups have used plane-wave-based pseudopotential methods, especially VASP,[35–37] to study the electronic structure and bulk elastic properties of spinel nitrides. We

 

TABLE I. Calculated properties of $\gamma$-$Sn_3N_4$ with comparison to $\gamma$-$Si_3N_4$ and $\gamma$-$Ge_3N_4$.

| | $\gamma$-$Sn_3N_4$ This work | Experiment | Other calculations | $\gamma$-$Si_3N_4$[b] | $\gamma$-$Ge_3N_4$[b] |
|---|---|---|---|---|---|
| Lattice constants | | | | | |
| $a$(Å) | 8.9544 | 9.037[a] | 8.96,[c]8.9651[d] | 7.8372 | 8.2110 |
| $u$ | 0.3839 | 0.3845 | 0.3844, 0.3845[d] | 0.3841 | |
| Band gap (eV) | 1.40 eV | | | 3.45 | 2.22 |
| Bandwidth (eV) | | | | | |
| Upper VB | 8.9 eV | | | 10.31 | 10.90 |
| N 2$s$ band | 4.30 eV | | | 5.70 | 5.61 |
| $m^*/m$ | 0.17 | | | 0.51 | 0.65 |
| $Q^*$ (electron) | | | | | |
| Cation (Sn, Si, Ge) | | | | | |
| Tetrahedral site | 2.66 | | | 2.65 | 2.81 |
| Octahedral site | 2.67 | | | 2.58 | 2.80 |
| N | 6.00 | | | 6.05 | 5.90 |
| BO (BL in Å) | | | | | |
| $Sn_{tet}$-N | 0.287 (2.077) | | | 0.362 (1.831) | 0.327 (1.907) |
| $Sn_{oct}$-N | 0.196 (2.162) | | | 0.241 (1.885) | 0.220 (1.982) |
| $B_0$ (GPa) and $B_0'$ | 187.2, 4.34 | | 186,[c]4.53[c] 203.6,[d]4.98[d] | 280.1, 3.76 | 286.6, 3.14 |
| $\varepsilon_1(0)$ | 6.8 | | | 4.7 | 6.5 |
| $\omega_p$ (eV) | 15.1 | | | 20.5 | 19.2 |

[a]Ref. 31.
[b]Ref. 7.
[c]Ref. 32.
[d]Ref. 11.

have now used VASP to calculate the structure and bulk properties of $\gamma$-$Sn_3N_4$ and compare them with the previous results obtained using the OLCAO method.[38] The VASP-optimized structure is then used for all other electronic and spectroscopic calculations using the OLCAO method. In the VASP calculation, we used the Perdew-Wang form of the generalized gradient approximation (GGA) for the exchange-correlation potential in the density functional theory and projected augmented wave pseudopotential. A high-kinetic-energy cutoff of 1000 eV was adopted such that the energy and residual force on each atom converge to 0.001 eV and 0.01 eV/Å, respectively. A Monkhorst-pack set of **k** points on an $8\times8\times8$ mesh was used for **k**-space sampling. For bulk properties calculation, we used a fixed-volume approach to obtain seven data points near the equilibrium volume $V_0$. The Birch-Murnaghan equation of state[39] (EOS) was used to obtain bulk modulus $B_0$ and its pressure coefficient $B_0'$ from the calculated total energy versus volume data. The use of other forms of EOS changes $B_0$ only slightly. The equilibrium lattice constant and the bulk modulus were obtained for $\gamma$-$Sn_3N_4$ from VASP calculation and are listed in Table I.

We have used the OLCAO method in previous studies of the electronic structure and bulk properties of spinel nitrides.[2,3,7,8,10,11] This is also a density-functional-theory-based method within the local density approximation (LDA) and has been extensively used by us to study a variety of crystalline[40–46] and noncrystalline[47,48] materials, complex microstructures such as grain boundaries,[49,50] and interfaces.[51] The method is particularly effective for complex structures where other first-principles methods may find some limitations. The details of the method have been described in many published papers and will not be repeated. The use of localized atomic orbitals in the basis expansion enables us to obtain information on charge transfer and interatomic bonding via effective atomic charges and bond order calculations using the Mulliken population analysis scheme.[52] In the present case, a full basis set consisting of Sn $(1s,2s,3s,4s,5s,6s,2p,3p,4p,5p,6p,3d,4d,5d)$ and N $(1s,2s,3s,2p,3p)$ atomic orbitals was adopted for the ground-state electronic structure calculation. The semicore 4$d$ states of Sn were treated as valence states to improve the accuracy. In addition, the linear optical properties within the random phase approximation of the theory for interband optical transitions can be easily calculated using the OLCAO method. For the optical properties and XANES calculations, additional orbitals were added to the full basis set (referred to as an extended basis set) to improve the accuracy of the higher unoccupied states. A large number of **k** points (408 **k** points on a $16\times16\times16$ mesh) in the irreducible portion of the Brillouin zone (BZ) was used for the electronic structure and linear optical calculations.

For the XANES-ELNES spectra calculation, we used the well-tested real-space supercell method[34] within the OLCAO

scheme. The method has been successfully applied to many crystals[53–60] in recent years with results in excellent agreement with measurements. We briefly describe the procedures involved in this calculation. A sufficiently large supercell must be used to minimize the artificial interactions between the core hole of the excited atom and its image in the adjacent periodic supercells. In contrast to the linear optical properties calculation, the XANES-ELNES calculation has different initial and final states. The initial state is the ground state of the supercell in which the core orbitals of the target atom are retained in the OLCAO formalism. The core orbitals of all other atoms in the supercell are eliminated by the orthogonalization process to reduce the size of the secular equation. The final state is the core-hole state in which an electron in the core orbital ($1s$ for the $K$ edge, $2p$ for the $L$ edge, and $3d$ for the $M$ edge) is removed and put at the lowest conduction band (CB). The Columbic interaction between the electron in the CB and the hole left behind is accounted for in the self-consistent iterations of the Kohn-Sham equation. Strictly speaking, this final state is not a one-electron state in the traditional sense because it includes the effect of the two-particle interactions between the electron and hole. This interaction drastically changes the crystal potential and the wave functions of the final unoccupied states to be very different from the unoccupied states in the ground-state calculation. The final spectrum is obtained by applying the usual Fermi's golden rule for electron transition from the initial (ground) state to the final (core-hole) state with the dipole approximation. The full inclusion of the dipole transition matrix automatically imposes the section rules for the transition. For the $K$ and $M$ edges, the XANES spectra probe the final CB-state wave function having the $p$ angular momentum character and, for the $L$ edge, the $(s+d)$ angular momentum character. The transition energy is obtained from the difference in the total energies of the ground-state and final-state calculations. To our knowledge, no other methods for XANES-ELNES calculations have this unique feature of obtaining the transition energy. In the present calculation for $\gamma$-$Sn_3N_4$, a $2\times2\times2$ supercell of 112 atoms was used which is sufficiently large such that the distance of separation between the core holes is at least 12.7 Å. In the current implementation, a Gaussian broadening of 1 eV at full width at half maximum (FWHM) is applied to all calculated spectra. This is to avoid using the broadening procedure itself as an artificial means to improve agreement with measured data. In reality, the experimentally measured curves will have different sources for broadening effect at different energy ranges. This aspect of the spectral interpretation has not been fully explored by us.

## III. RESULTS AND DISCUSSIONS

### A. Bulk properties

Based on the VASP calculation, we have obtained the lattice constant of $a=b=c=8.9544$ Å and the internal parameter of $u=0.3839$ which differs from the measured values[31] by less than 1% and 0.16%, respectively. They are almost identical to the other VASP calculation[32] and almost the same as earlier calculations using the OLCAO method.[11] It is somewhat surprising to see such close agreement in the crystal parameters since in VASP, the GGA was used for the exchange-correlation potential, while in OLCAO, the LDA was used. Generally speaking, within the same computational method, the GGA tends to give a large lattice constant than the LDA. In the present case, other differences such as differet types of basis expansion may have an offsetting effect, resulting in a fortuitous agreement between the geometries obtained from the two different methods and approaches. Since the major focus of this paper is to present the results of $\gamma$-$Sn_3N_4$ and not specific comparisons between different methods and potentials, no additional tests were carried out. Even if such lengthy tests were done, there are still other uncertainties related to the choice of energy cutoff in the VASP calculation and the type of basis set used in the OLCAO calculation.

The bulk modulus and the pressure coefficient of $\gamma$-$Sn_3N_4$ have been calculated before[11] using the OLCAO method with an efficient geometry optimization scheme.[61] We obtained values of $B_0=203.6$ GPa and $B_0'=4.98$. In the present case, we repeated the bulk properties calculation using VASP. The total energies of compressed and dilated cells at the seven different volumes were obtained after full relaxation. The Birch-Murnaghan EOS (Ref. 39) was used to fit the $E$-$V$ data, and we obtained $B_0=187.2$ GPa and $B_0'=4.34$. The close agreement of the bulk modulus obtained by two very different computational methods gives us confidence in the accuracy of both calculations. Compared with similar bulk properties data for $\gamma$-$Si_3N_4$ and $\gamma$-$Ge_3N_4$ calculated by the OLCAO total energy minimizations scheme,[7] we observe a clear trend in the reduction of bulk modulus $B_0$ from 280.1 GPa in $\gamma$-$Si_3N_4$ to 268.6 GPa in $\gamma$-$Ge_3N_4$ and to 187.2 GPa in $\gamma$-$Sn_3N_4$. Obviously, the reduced bulk modulus, or smaller hardness, is related to the weaker Sn-N bond as compared to the Si-N and Ge-N bonds and as indicated by their BO values (see subsection B below). Our calculated $B_0$ for $\gamma$-$Sn_3N_4$ is also in excellent agreement with the calculation reported in Ref. 29. They obtained $B_0=186$ GPa and $B_0'=4.53$.

### B. Electronic structure and bonding

The electronic structure and bonding of $\gamma$-$Sn_3N_4$ were calculated using the OLCAO method based on the VASP-relaxed crystal structure. Figure 1 shows the calculated band structure of $\gamma$-$Sn_3N_4$. Similar to other group-IVB spinel nitrides, it is an insulator with a direct band gap of 1.40 eV at $\Gamma$. This is considerably smaller than the band gaps of $\gamma$-$Si_3N_4$ (3.45 eV) and $\gamma$-$Ge_3N_4$ (2.22 eV).[2,7] The real band gap could be slightly larger since the LDA used in the calculation tends to underestimate the real band gap in insulators. Like $\gamma$-$Si_3N_4$ and $\gamma$-$Ge_3N_4$, the top of the valence band (VB) in $\gamma$-$Sn_3N_4$ is very flat, indicating a large hole effective mass. Unlike $\gamma$-$Si_3N_4$ and $\gamma$-$Ge_3N_4$, the bottom of the CB consists of a single band that is predominately N $3s$ in character. The electron effective mass of this band at the CB minimum is only 0.17, much smaller than the effective mass of 0.51 and 0.65 for $\gamma$-$Si_3N_4$ and $\gamma$-$Ge_3N_4$, respectively, and is comparable to that of GaN ($\sim$0.19) and AlP ($\sim$0.13). This

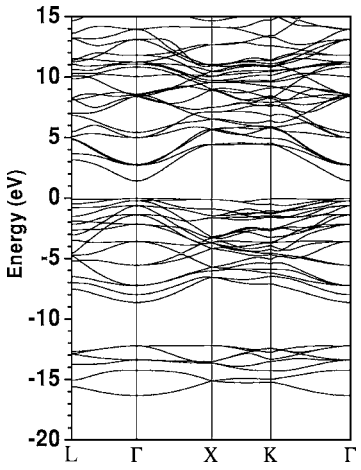


FIG. 1. Calculated band structure of $\gamma$-$Sn_3N_4$.

could imply that $\gamma$-$Sn_3N_4$ may find interesting applications in microelectronics technology.

The calculated total density of states (TDOS) and atom-resolved partial density of states (PDOS) are shown in Fig. 2. Like $\gamma$-$Si_3N_4$ and $\gamma$-$Ge_3N_4$, there are noticeable differences in the PDOS of Sn at the octahedral site ($Sn_{oct}$) and the tetrahedral site ($Sn_{tet}$). In the narrow region at the top of the VB where the main contribution comes from the N 2*s* non-bonding orbital that is responsible for the flat VB, $Sn_{oct}$ has a much larger contribution than $Sn_{tet}$. On the other hand, $Sn_{tet}$ has a greater presence in the states near the CB edge. The single band near the bottom of the CB is predominately from the N 3*s* orbitals.

There are many well-resolved sharp structures in the DOS of $\gamma$-$Sn_3N_4$. In the upper VB (from 0 to −8.9 eV) which is dominated by N 2*p* orbitals, seven distinct peaks (labeled as V1 to V7 in Fig. 2) at −0.1, −1.0, −1.5, −2.7, −3.7, −4.9, and −6.7 eV can be identified. This is to be compared with only three (six) sharp peaks in the same energy range for $\gamma$-$Si_3N_4$ ($\gamma$-$Ge_3N_4$). In particular, the sharpest peak, V1, is at the top of the VB and is consistent with the flat topped VB. The lower VB of predominately N 2*s* in composition and has a width of 4.3 eV. The DOS at the CB edge in $\gamma$-$Sn_3N_4$ shows a footlike feature originating from the single lowest CB discussed above. This feature is different from $\gamma$-$Si_3N_4$ and $\gamma$-$Ge_3N_4$ where the CB edge consists of orbitals of the cations and rises more steeply. We will return to this point later in the discussion of optical absorption edge. The CB DOS is also rich in structures. To facilitate later discussion, we label the major peaks in the first 13 eV range as C1, C2, C3, and C4. C1 and C2 are well-defined peaks at 4.4 eV and 5.8 eV, respectively. C3 and C4 each consists of a group of sharp peaks with the centroids located at 8.1 eV and 10.6 eV, respectively. The multiple peak structures have contributions from all three sites of the spinel lattice, except for C4 which has contributions mostly from $Sn_{oct}$ and N. This later feature is similar to $\gamma$-$Ge_3N_4$ but different from $\gamma$-$Si_3N_4$, indicating different electron states around 11 eV in $\gamma$-$Si_3N_4$.

The calculated Mulliken effective charges $Q^*$ and the bond order (BO) between cation and anion are listed in Table I. The $Q^*$ for Sn at $Sn_{tet}$ and $Sn_{oct}$ are 2.65 and 2.58 electrons,

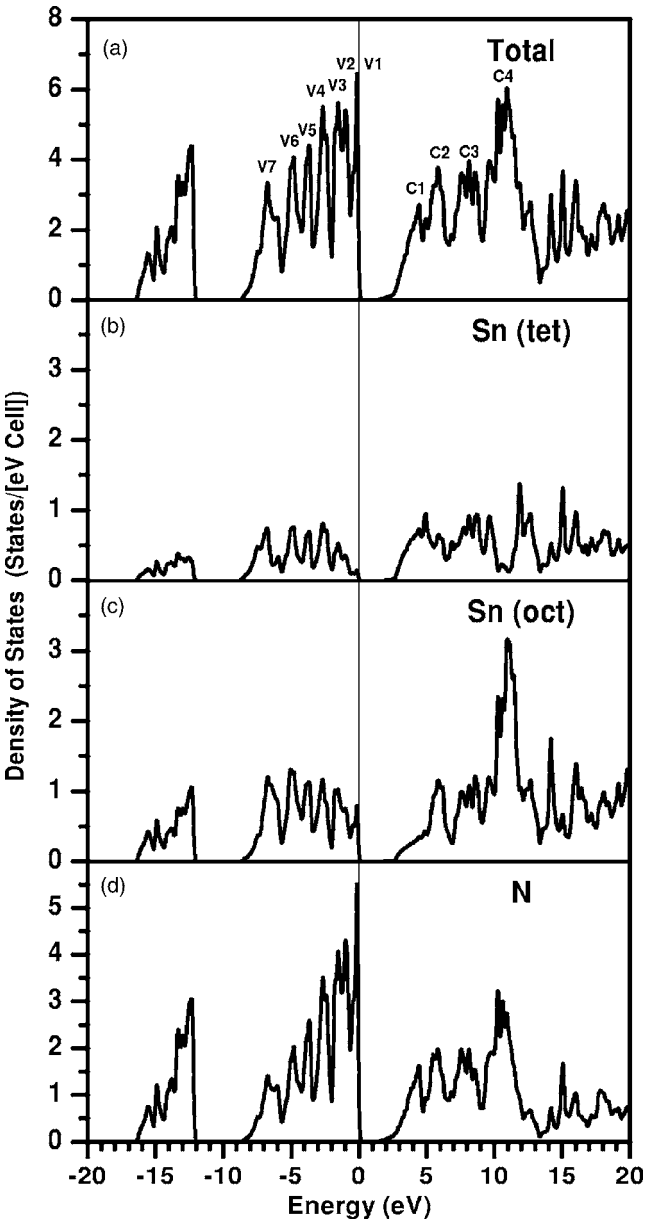


FIG. 2. Calculated total and partial DOS of $\gamma$-$Sn_3N_4$.

respectively, while $Q^*$ for N is 6.00 electrons. These effective charge numbers are somewhere between the $Q^*$ values in $\gamma$-$Si_3N_4$ and $\gamma$-$Ge_3N_4$ which have corresponding values for cation and N of 2.65, 2.58, and 6.05 for $\gamma$-$Si_3N_4$ and 2.81, 2.80, and 5.90 for $\gamma$-$Ge_3N_4$. So the relative values of the effective charges for the cation at the octahedral site and the tetrahedral site are quite close in both $\gamma$-$Sn_3N_4$ and $\gamma$-$Ge_3N_4$ while the $Q^*$ values of $Si_{tet}$ is somewhat larger than $Si_{oct}$. This could be related to the fact that in $\gamma$-$Ge_3N_4$ and $\gamma$-$Sn_3N_4$, the semicore Ge 3*d* and Sn 4*d* were taken as the valence orbitals in the OLCAO calculation. These semicore *d* orbitals apparently have non-negligible overlap integrals with the valence orbitals of the neighboring atoms based on which the $Q^*$ values were calculated (the $Q^*$ values of Sn and Ge exclude the ten *d* electrons). In Si, there is no such occupied inner *d* orbitals. It is also well known that the Mulliken population analysis depends on the basis set used.

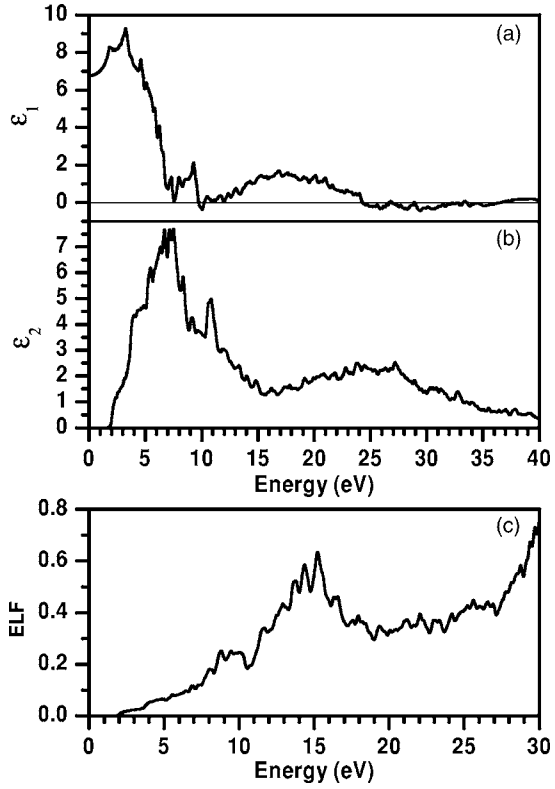


FIG. 3. Optical properties of $\gamma$-$Sn_3N_4$: (a) real dielectric function, (b) imaginary dielectric function, and (c) energy loss function.

While it is meaningful to compare the $Q^*$ at the octahedral and tetrahedral sites of the cations in the same spinel lattice, the comparison among the three different crystals becomes less meaningful since the atomic bases used for Si, Ge, and Sn are different.

The BO value is a different story. The BO for $Sn_{tet}$-N and $Sn_{oct}$-N are 0.287 and 0.196, respectively, considerably smaller than the corresponding BO values in $\gamma$-$Si_3N_4$ and $\gamma$-$Ge_3N_4$ (see Table I). The main reason is that the bond lengths (BLs) in $\gamma$-$Sn_3N_4$ are much longer because of the larger ionic size of Sn and the larger lattice constant. Still the BO values between Sn and N are much larger than the BO in oxides, indicating stronger covalent bonding in spinel nitrides in general. However, the difference in the cation basis set may add to some of the differences, so these BO numbers have to be treated with some caution.

### C. Optical properties

The calculated optical properties of $\gamma$-$Sn_3N_4$ in the form of the complex frequency-dependent dielectric function and the electron energy loss function are shown in Fig. 3. We will focus our discussion on the imaginary dielectric function $\varepsilon_2(\hbar\omega)$. The general feature of the optical absorption curve is similar to $\gamma$-$Si_3N_4$ and $\gamma$-$Ge_3N_4$ (Fig. 5 of Ref. 7). However, $\gamma$-$Sn_3N_4$ has many more absorption peaks because of the increased number of peak structures in both the VB and CB. The main absorption peak is at 7.0 eV compared to the same peak at 9.9 eV in $\gamma$-$Si_3N_4$ and 7.8 eV in $\gamma$-$Ge_3N_4$. So there is a systematic shift towards lower energy from $\gamma$-$Si_3N_4$ to $\gamma$-$Ge_3N_4$ and to $\gamma$-$Sn_3N_4$. Unlike $\gamma$-$Si_3N_4$, $\gamma$-$Sn_3N_4$ also has another prominent peak at 10.1 eV above the main peak. This same peak is recognizable but less prominent in $\gamma$-$Ge_3N_4$ at 11.7 eV. From the positions of various sharp peak structures in the VB and CB, it is likely that this sharp peak at 10.1 eV originates from transitions from V1 to C4 because of the resemblance of the C4 structure in the CB of $\gamma$-$Sn_3N_4$ and $\gamma$-$Ge_3N_4$ discussed before. But contributions from V6 to C2 and V5 to C3 are also possible. At a higher-absorption-energy range, $\gamma$-$Sn_3N_4$ has a broad peak centered at about 25 eV. No such broad higher peak exists in $\gamma$-$Si_3N_4$ and $\gamma$-$Ge_3N_4$.

An important difference in the absorption curve of $\gamma$-$Sn_3N_4$ and that of the other two spinel nitrides is the absorption edge. In $\gamma$-$Si_3N_4$ and $\gamma$-$Ge_3N_4$, the absorption edges are close to the calculated direct band gap since they simply reflect the direct interband transitions at the $\Gamma$ point. In $\gamma$-$Sn_3N_4$, the same interband transition at $\Gamma$ is either symmetry forbidden or has too small DOS amplitude at the CB minimum due to the footlike feature discussed above. As a result, the absorption edge in $\gamma$-$Sn_3N_4$ appears to be at 2.0 eV, much higher than the direct band-gap value of 1.40 eV. There are also broader shoulderlike structures at 2.5 eV and 4.5 eV in $\gamma$-$Sn_3N_4$. Therefore, a different symmetry and characteristic of the CB minimum in $\gamma$-$Sn_3N_4$ resulted in a very different absorption edge from that of $\gamma$-$Si_3N_4$ and $\gamma$-$Ge_3N_4$.

The calculated optical dielectric constant $\varepsilon_1(0)$ of $\gamma$-$Sn_3N_4$ is 6.4 which is slightly larger than that of $\gamma$-$Si_3N_4$ (4.7) and comparable to $\gamma$-$Ge_3N_4$ (6.5), so there is no obvious trend in three crystals. Much of this depends on the complex interplay of the band gap value, absorption edge, and specific features in the absorption curve. But like many other properties, $\gamma$-$Sn_3N_4$ is closer to $\gamma$-$Ge_3N_4$ than to $\gamma$-$Si_3N_4$ and, most likely, this is due to the absence of the inner atomic *d* shells in Si. On the other hand, the plasmon frequency $\omega_p$ identified as the broad peak in the electron-energy-loss function [Fig. 3(c)], which describes the frequency of collective excitation of the valence electrons, shows a consistent trend in going from $\gamma$-$Si_3N_4$ to $\gamma$-$Ge_3N_4$ to $\gamma$-$Sn_3N_4$. They are at 20.5 eV, 19.2 eV, and 15.1 eV respectively.

### D. XANES/ELNES spectra

XANES and/or ELNES spectroscopy is an important technique for modern materials characterization. It is generally regarded as the best way to understand the electronic structure of the unoccupied states in solids.[62,63] However, the analysis of such spectra and their proper interpretation has never been an easy task.[64] With the aid of credible theoretical calculations, the work can be made considerably easier. In spinel nitrides, only the N *K* and the Si $L_{2,3}$ edges of $\gamma$-$Si_3N_4$ have been measured using samples recovered from the shock-wave compression method.[23] Very recently, the measurement of the Ge *K* edge in $\gamma$-$Ge_3N_4$ was reported.[65] The lack of such measurements in spinel nitrides is partly attributed to the lack of pure single-phase samples of sufficient quantity. In general, shock-wave compression can pro-

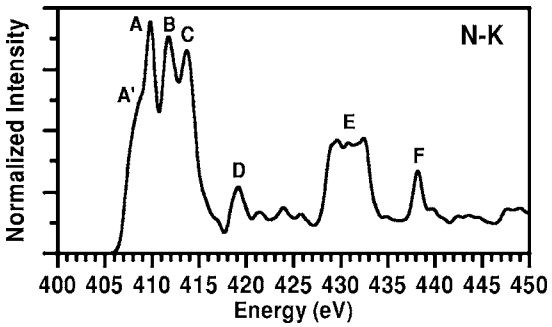


FIG. 4. Calculated N $K$ edge in $\gamma$-$Sn_3N_4$.

duce much larger quantities of spinel nitrides than those obtained from laser-heated annealing in a diamond anvil cell, but they are usually in powder form with somewhat reduced crystallinity. On the computational side, the XANES and ELNES spectra of $\gamma$-$Si_3N_4$ have been calculated using the supercell method.[23,55] The results show excellent agreement with the experimental data. It was shown that the spectra of $\gamma$-$Si_3N_4$ are very different from those of the hexagonal phases of $Si_3N_4$ ($\alpha$-$Si_3N_4$ and $\beta$-$Si_3N_4$).[55] The same rigorous calculation applied to $\gamma$-$Sn_3N_4$ will have predictive value that can be used for future comparison with experimental measurements. Furthermore, Sn is a much heavier atom. In the past, most of the XANES calculations have been restricted to lighter elements in the second or third row of the periodic table. Here we report not only the N $K$ edge, but also the Sn $K$, Sn $L_3$, and Sn $M_5$ edges in $\gamma$-$Sn_3N_4$ for energy ranges up to 45 eV from the edge onset. In particular, the differences between the spectra from the tetrahedral site and the octahedral site are clearly demonstrated. Experimentally, the measured spectrum for a specific element is the combined spectrum from different sites of the same atom. We will discuss these spectra individually below. The energy scales in these spectra are the theoretical values obtained from the differences in the total energies as explained before. They are supposed to be close to the experimental energy scales.

#### *1. N K edge*

The calculated N $K$ edge in $\gamma$-$Sn_3N_4$ is shown in Fig. 4. The spectrum is very rich in structures. We divide it into two regions: Region I covers the first 10 eV from the edge onset and region II covers the energy range above region I. In region I, the spectrum has three peaks labeled $A$,$B$, and $C$ and a shoulder labeled $A'$. The spectrum has some resemblance to the N $K$ edge in $\gamma$-$Si_3N_4$ (Ref. 23) where there are also three peaks and a shoulder but with slightly different positions and amplitude. It is not totally clear if these four structures are related to peaks C1–C4 in the CB PDOS of N since the XANES spectrum can be significantly affected by the core-hole interaction and the matrix elements of transitions. In region II, there are two prominent peaks $D$ and $F$ at 419.0 eV and 438.1 eV, respectively, and a plateaulike structure $E$ between 429.0 eV and 432.5 eV. The positions of these peaks are listed in Table II.

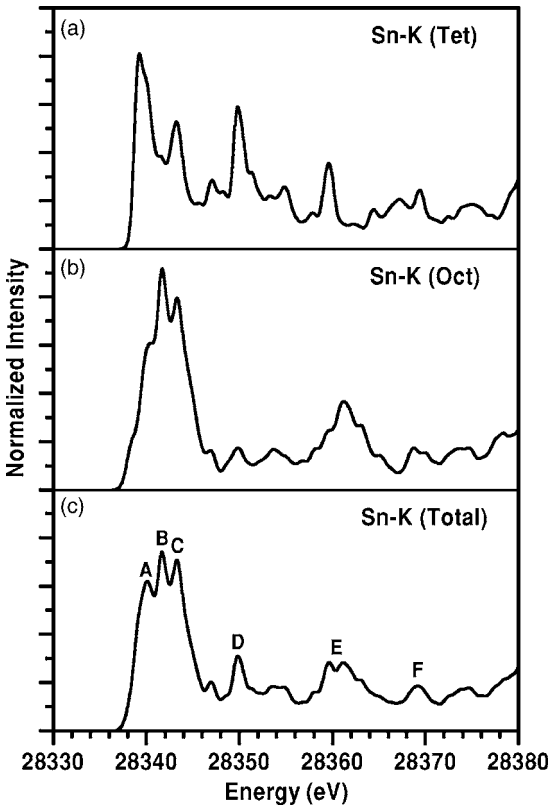


FIG. 5. Calculated Sn $K$ edge in $\gamma$-$Sn_3N_4$: (a) tetrahedral site, (b) octahedral site, and (c) total.

#### *2. Sn K edge*

The calculated Sn $K$ edge in $\gamma$-$Sn_3N_4$ is shown in Fig. 5. There are marked differences between the spectra from the $Sn_{tet}$ and $Sn_{oct}$. In the former, the leading peak at the edge onset is very sharp and, in the latter, the leading feature is a shoulder. The energies of the edge onset for the two spectra are also slightly different, 28 337.5 eV for $Sn_{tet}$ and 28 336.6 eV for $Sn_{oct}$. Any experimental measurement is unlikely to resolve the difference between the two spectra. The com-

TABLE II. Positions of major peaks in the calculated XANES and ELNES spectra in $\gamma$-$Sn_3N_4$.

| Edge | Peak position (eV) | | | | | |
|---|---|---|---|---|---|---|
| N $K$ | $A'$(408.1) | $A$ (409.4) | $B$(410.3) | $C$(413.0) | $D$(419.0) | $E$(429.0–432.5) F(438.1) |
| Sn $K$ | $A$ (28340) | $B$(28341.8) | $C$(28343.2) | $D$(28350) | $E$(28359.8,28361.6) | $F$(28369.3) |
| Sn $L_3$ | $A$ (3974) | $B$(3980) | $C$(3986.1) | $D$(3994.2) | $E$(3997.3) | |
| Sn $M_5$ | $A$ (518.5) | $B$(520.2) | $C$(521.9) | $D$(528.0) | $E$(538.1,540.0,541.8) | $F$(547.5) |

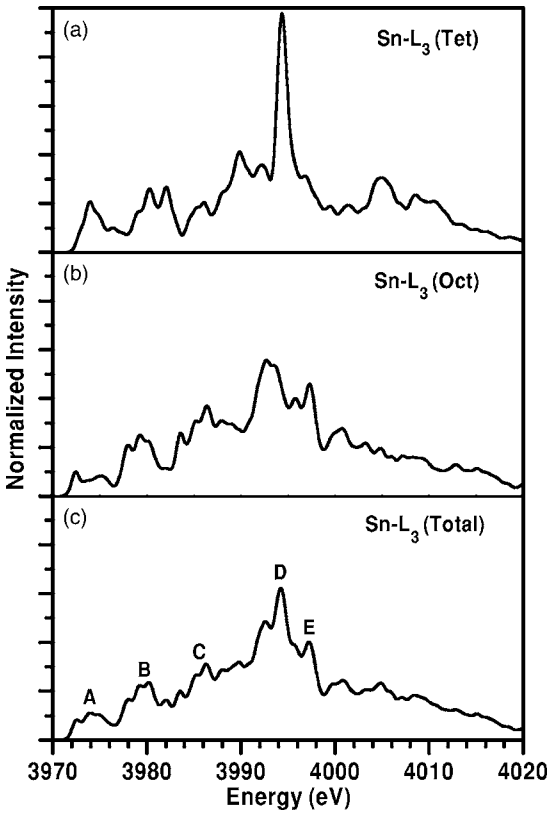


FIG. 6. Calculated Sn $L_3$ edge in $\gamma$-$Sn_3N_4$: (a) tetrahedral site, (b) octahedral site, and (c) total.

bined spectrum in the ratio of 1:2 for $Sn_{tet}$ to $Sn_{oct}$ is shown in Fig. 6(c) with major peaks labeled from *A* to *F*. Because of the slightly different edge onset, the combined spectrum is different from the spectra of either $Sn_{tet}$ or $Sn_{oct}$ although similar major peaks can be identified. In the first 8 eV from the edge onset, the combined spectrum has three peaks $A,B$, and $C$ at 28 340 eV, 28 341.8 eV, and 28 343.2 eV, respectively. In the higher-energy region, there is a peak $D$ at 28350 eV originating from $Sn_{tet}$ and a double peak $E$ at 28 359.8 eV and 28 361.6 eV coming from the combination of similar peaks at the two Sn sites. There is a less prominent peak $F$ at 28 369.3 eV. These peak positions are listed in Table II.

#### *3. Sn* $L_3$ *edge*

The XANES $L_{2,3}$ edge probes the transition from the $2p$ core level to the CB. Since spin-orbit splitting is not included in the present calculation, the usual $L_{2,3}$ edges reduce to only the $L_3$ edge. This should not be of much concern since the $L_3$ edge in Sn is well separated from $L_2$ by about 127 eV. In metallic systems with partially occupied $d$ electrons, proper treatment of $L_{2,3}$ will be very important and may require methods beyond the one-electron calculations.[64] The calculated Sn $L_3$ edge in $\gamma$-$Sn_3N_4$ is shown in Fig. 6. Again our discussion will focus on the combined spectrum from $Sn_{tet}$ and $Sn_{oct}$ with weighting factors of 1 and 2, respectively. There are some differences in the spectra from the two different sites but not as large as in the Sn *K* edges. The most

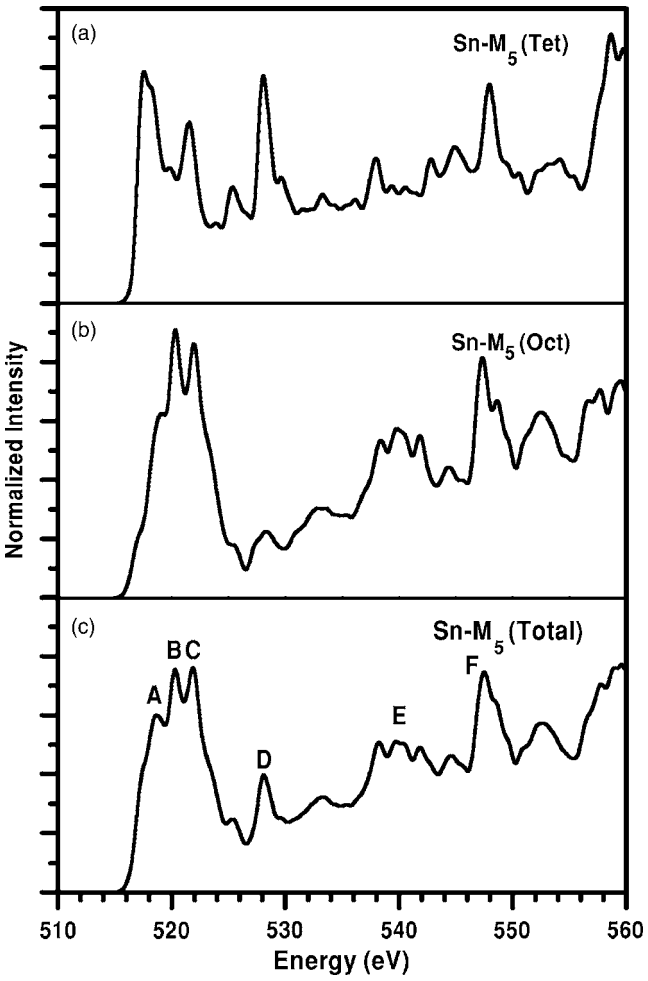


FIG. 7. Calculated Sn $M_5$ edge in $\gamma$-$Sn_3N_4$: (a) tetrahedral site, (b) octahedral site, and (c) total.

prominent peak is the peak $D$ at 3994.2 eV which is inherited mostly from the sharp peak at the same energy in $Sn_{tet}$. The other peaks $(A,B,C,E)$ are less prominent and could be due to the fact that the Sn $(s+d)$ states in the unoccupied bands are relatively delocalized. There is also a slight difference in the onset energies, 3971.7 eV for the $Sn_{tet}$ and 3971.0 eV for $Sn_{oct}$, which could also contribute to the less sharp peak structures in the combined spectrum. The various peak positions are listed in Table II.

#### *4. Sn* $M_5$ *edge*

The calculated Sn $M_5$ edge in $\gamma$-$Sn_3N_4$ is shown in Fig. 7. The $M_{4,5}$ edge probes transitions from the $3d$ core to the empty CB. There should be two edges $M_5$ and $M_4$ corresponding to two different core levels with different total angular momentum $j=5/2$ and $3/2$ when spin-orbit coupling is taken into account. In the present calculation without spin-orbit coupling, only the $M_5$ spectrum is calculated. Nevertheless, the $M_5$ spectrum provides useful insights for our discussion. Since the transitions from the $3d$ core level to the CB are suppose to probe the angular momentum states of with $p$ character, similar to the Sn *K* edge, the Sn $M_5$ edge should be close to the Sn *K* edge. This is indeed the case. The spectra

in Fig. 7 are very similar to the spectra of Fig. 5 except that they have different energy scales because of the different core levels. It is noted that the $M_5$ edge has a smooth gradually increasing background as the energy is increased. This can be explained in terms of the difference in the initial core states. In the *K* edge, the 1*s* core is deep and exceptionally sharp. In the 3*d* core, there are five levels (spin nonresolved) and are less deep. The matrix elements of coupling have different overlaps with larger values for the 3*d* to CB transitions than for the 1*s* to the CB transitions, resulting in a gradual increase in the spectral amplitude. The peak positions of the $M_5$ edge are also listed in Table II. It can be verified that the relative separations of the peaks in the $M_5$ edge are very close to that of the *K* edge.

## IV. SUMMARY

In this paper, we have presented detailed information on the electronic structure, bulk properties, and spectroscopic properties of spinel tin nitride $\gamma$-$Sn_3N_4$. Two well-tested methods VASP and OLCAO were used, and the results obtained from these two very different methods were essentially consistent. In comparison with the other two binary spinel nitrides $\gamma$-$Si_3N_4$ and $\gamma$-$Ge_3N_4$, a clear trend in the increasing size of the cation can be established. $\gamma$-$Sn_3N_4$ has a smaller band gap, less strong bonds, a smaller bulk modules, and a lower plasmon frequency. There are cases such as in the PDOS and Mulliken effective charges, and features in the optical spectra, results from $\gamma$-$Sn_3N_4$ are closer to $\gamma$-$Ge_3N_4$ than to $\gamma$-$Si_3N_4$. This is interpreted in terms of the absence of the inner semicorelike *d* states in Si of $\gamma$-$Si_3N_4$ which result in somewhat different electronic structure and bonding. In $\gamma$-$Sn_3N_4$, the bonds between Sn and N at both sites are weaker than the similar cation-N bonds in $\gamma$-$Si_3N_4$ and $\gamma$-$Ge_3N_4$ because of the longer bond lengths. Its optical dielectric constant, however, is close to the other two crystals. The optical properties of $\gamma$-$Sn_3N_4$ differ from the other two crystals near the absorption edge because of the footlike structure due to a single conduction band of N 3*s* character. This is in contrast to the optical absorptions in $\gamma$-$Si_3N_4$ and $\gamma$-$Ge_3N_4$ where the states at the CB minimum come mainly from the cations. This single band at the CB minimum has an effective mass of only 0.17 which makes $\gamma$-$Sn_3N_4$ an attractive semiconductor suitable for many potential applications in modern technology. The calculation of the N *K*, Sn *K*, Sn $L_3$, and Sn $M_5$ spectra revealed rich structures in the spectra of this crystal. They show marked differences between the spectrum for Sn at the tetrahedral and octahedral sites. The combined spectrum will be the one that can be meaningfully compared with experiment and is different from the spectra at the specific sites. This underscores the importance of having theoretical input in the interpretation of the XANES and ELNES spectra for materials characterization. We have also demonstrated the resemblance in the spectra of the Sn *K* and Sn $M_5$ edges as required by the quantum-mechanical selection rule. There is a gradual increase in the background in the Sn $M_5$ spectrum due to the difference in the initial orbital state of the core atom. We hope our detailed calculation will stimulate additional experiment on this interesting material that may find useful applications. It is also noted that so far we are unable to provide a more detailed interpretation of various peaks in the XANES and ELNES spectra. It might be possible to calculate the energy-dependent bond-order values for a specific pair of atoms in the conduction band and compare that with the calculated absorption curves or use complicated graphic displays to show the composition of the wave functions of the states associated with the peak structures. However, it appears that such detailed and rather cumbersome analysis will be premature in the absence of experimentally measured spectra.

## ACKNOWLEDGMENTS

This work is supported by the U.S. Department of Energy under the Grant No. DE-FG02-84DR45170. This research used the resources of NERSC supported by the Office of Basic Science of the DOE under Contract No. DE-AC03-76SF00098.

[1] A. Zerr, G. Miege, G. Serghiou, M. Schwarz, E. Kroke, R. Riedel, H. Fuess, P. Kroll, and R. Boehler, Nature (London) **400**, 340 (1999).
[2] S.-D. Mo, L. Ouyang, W. Y. Ching, I. Tanaka, Y. Koyama, and R. Riedel, Phys. Rev. Lett. **83**, 24 (1999).
[3] W. Y. Ching, S-D. Mo, L. Ouyang, I. Tanaka, and M. Yoshiya, Phys. Rev. B **61** 10609 (2000).
[4] J. E. Lowther, Phys. Rev. B **62**, 5 (2000).
[5] J. J. Dong, O. F. Sankey, S. K. Deb, G. Wolf, and P. F. McMillan, Phys. Rev. B **61**, 11979 (2000).
[6] D. Bagayoko and G. L. Zhao, Physica C **364**, 261 (2001).
[7] W. Y. Ching, S.-D. Mo, and L. Ouyang, Phys. Rev. B **63**, 245110 (2001).
[8] W.-Y. Ching, S.-D. Mo, I. Tanaka, and M. Yoshiya, Phys. Rev. B **63**, 064102 (2001).
[9] J. M. Recio, R. Franco, A. Martín Pendas, M. A. Blanco, L. Pueyo, and R. Pandey, Phys. Rev. B **63**, 184101 (2001).
[10] W. Y. Ching, L. Ouyang, and J. Gale, Phys. Rev. B **61**, 8696 (2000).
[11] W. Y. Ching, S-D. Mo, L. Ouyang, P. Rulis, I. Tanaka, and M. Yoshiya, J. Am. Ceram. Soc. **85**, 75 (2002).
[12] J. Dong, J. Deslippe, O. F. Sankey, E. Soignard, and P. F. McMilliam, Phys. Rev. B **67**, 094104 (2003).
[13] P. Kroll, J. Solid State Chem. **176**, 530 (2003).
[14] C. M. Fang, G. A. de Wijs, H. T. Hintzen, and G. J. de With, J. Appl. Phys. **93**, 5175 (2003).
[15] P. Mori-Sanches, M. Marques, A. Beltran, J. Z. Jiang, L. Gerward, and J. M. Recio, Phys. Rev. B **68**, 064115 (2003).
[16] W. Paszkowicz, R. Minikayev, P. Piszora, M. Knapp, C. Bähtz, J. M. Reico, M. Margués, P. Mori-Sánches, L. Gerward, and J. Z. Jiang, Phys. Rev. B **69**, 052103 (2004).
[17] C. Kocer, N. Horosaki, and S. Ogata, Phys. Rev. B **67**, 035210

(2003).
[18] G. Serghiou, G. Miehe, O. Tschauner, A. Zerr, and R. Boehler, J. Chem. Phys. **111**, 4659 (1999).
[19] K. Leinenweber, M. O'Keefe, M. S. Somayazulu, H. Hubert, P. F. McMillan, and G. H. Wolf, Chem.-Eur. J. **5**, 3076 (1999).
[20] J. Z. Jiang, K. Stahl, R. W. Berg, D. J. Frost, T. J. Zhou, and P. X. Shi, Europhys. Lett. **51**, 62 (2000).
[21] M. Shwarz, G. Moehe, A. Zerr, E. Korke, B. T. Poe, H. Fuess, and R. Riedel, Adv. Mater. **12**, 883 (2000).
[22] H. He, T. Sekine, T. Kobayashi, H. Hirosaki, and I. Suzuki, Phys. Rev. B **62**, 11412 (2000).
[23] I. Tanaka, T. Mizoguchi, T. Sekine, H. He, K. Kimoto, S.-D. Mo, and W. Y. Ching, Appl. Phys. Lett. **78**, 2134 (2001).
[24] E. Soignard, M. Somayazulu, H.-K. Mao, J. Dong, O. F. Sankey, and P. F. McMillam, Solid State Commun. **120**, 237 (2001); E. Soignard, M. Somayazulu, J. Dong, O. F. Sankey, and P. F. McMillan, J. Phys.: Condens. Matter **13** 557 (2001).
[25] I. Tanaka, F. Oba, T. Sekine, E. Ito, A. Kubo, K. Tasumi, A. Adachi, and T. Yamamoto, J. Mater. Res. **17**, 731 (2002).
[26] J. Z. Jiang, F. Kragh, D. J. Frost, K. Stahl, and H. Lindelov, J. Phys.: Condens. Matter **13**, L515 (2001); J. Z. Jiang, H. Lindelov, L. Gerward, K. Stahl, J. M. Reico, P. Mori-Sanchez, S. Carlson, M. Mezouar, E. Dooryhee, A. Fitch, and D. J. Frost, Phys. Rev. B **65**, 161202 (2002).
[27] A. Zerr, M. Kempf, G. Miege, M. Schwarz, E. Kroke, M. Goken, and R. Riedel, J. Am. Ceram. Soc. **85**, 8690 (2002).
[28] E. Soignard and P. F. McMillam, Chem. Mater. **16**, 3533 (2004).
[29] E. Soignard, P. F. McMillam, and K. Leinenweber, Chem. Mater. **16**, 5344 (2004).
[30] S. Leitch, A. Moewes, L. Ouyang, W. Y. Ching, and T. Sekine, J. Phys.: Condens. Matter **16**, 6469 (2004).
[31] M. Shemkunas, G. H. Wolf, K. Leinenweber, and W. T. Petuskey, J. Am. Ceram. Soc. **85**, 101 (2002).
[32] M. Shemkunas, W. T. Petuskey, A. V. G. Chizmeshya, K. Leinenweber, and G. H. Wolf, J. Mater. Res. **19**, 1392 (2004).
[33] N. Scotti, W. Kockelmann, J. Senker, S. Trassel, and H. Jacobs, Z. Anorg. Allg. Chem. **625**, 1435 (1999).
[34] Shang-Di Mo and W. Y. Ching, Phys. Rev. B **62**, 7901 (2000).
[35] G. Kresse and J. Hafner, Phys. Rev. B **47**, 558 (1993).
[36] G. Kresse and J. Furthmuller. Comput. Mater. Sci. **6**, 15 (1996).
[37] G. Kresse and J. Furthmuller, Phys. Rev. B **54**, 11169 (1996).
[38] W. Y. Ching, J. Am. Ceram. Soc. **73**, 3135 (1990).
[39] F. Birch, J. Geophys. Res. **83**, 1257 (1978).
[40] Yong-Nian Xu, W. Y. Ching, and B. K. Brickeen, Phys. Rev. B **61**, 1817 (2000); W. Y. Ching, Y.-N. Xu, and B. K. Brickeen, *ibid.* **63**, 115101 (2001).
[41] W. Y. Ching, Ming-Zhu Huang, and Shang-Di Mo, J. Am. Ceram. Soc. **83**, 780 (2000).
[42] W. Y. Ching, Yong-Nian Xu, and L. Ouyang, Phys. Rev. B **66**, 235106 (2002).
[43] Paul Rulis, Lizhi Ouyang, and W. Y. Ching, Phys. Rev. B **70**, 155104 (2004).
[44] W. Y. Ching, L. Ouyang, and Yong-Nian Xu, Phys. Rev. B **67**, 245108 (2003).
[45] W. Y. Ching, L. Ouyang, Hongzhi Yao, and Y.-N. Xu, Phys. Rev. B **70**, 085105, (2004).
[46] W. Y. Ching, J. Am. Ceram. Soc. **87**, 1996 (2004).
[47] M.-Z. Huang and W. Y. Ching, Phys. Rev. B **54**, 5299 (1996); Ming-Zhu Huang, Lizhi Ouyang, and W. Y. Ching, *ibid.* **59**, 3540 (1999).
[48] Lizhi Ouyang and W. Y. Ching, J. Appl. Phys. **95** 7918 (2004).
[49] Shang-Di Mo, W. Y. Ching, M. Chelshim, and G. Duscher, Phys. Rev. B **60**, 2416 (1999).
[50] Jun Chen, Yong-Nian Xu, Paul Rulis, Lizhi Ouyang, and W. Y. Ching, Acta Mater. **53**, 403 (2005).
[51] Paul Rulis, Jun Chen, Lizhi Ouyang, W. Y. Ching, Xiaotao Su, and S. H. Garofalini, Phys. Rev. B **71**, 235317 (2005).
[52] R. S. Mulliken, J. Am. Chem. Soc. **23**, 1833 (1955); R. S. Mulliken, *ibid.* **23**, 1841 (1955).
[53] S. D. Mo and W. Y. Ching, Appl. Phys. Lett. **78**, 3809 (2001).
[54] I. Tanaka, T. Mizoguchi, T. Sekine, H. He, K. Kimoto, S.-D. Mo, and W. Y. Ching, Appl. Phys. Lett. **78**, 2134 (2001).
[55] W. Y. Ching, Shang-Di Mo, and Yu Chen, J. Am. Chem. Soc. **85**, 11 (2002).
[56] Y.-N. Xu, Yu Chen, Shang-Di Mo, and W. Y. Ching, Phys. Rev. B **65**, 235105 (2002).
[57] I. Tanaka, T. Mizoguchi, M. Matsui, S. Yoshioka, F. Oba, H. Adachi, T. Okajima, M. Umesaki, W. Y. Ching, Y. Inoue, M. Mizuno, and Y. Shirai, Nat. Mater. **2**, 541 (2003).
[58] T. Mizoguchi, I. Tanaka, S. Yoshioka, M. Kunisu, T. Yamamoto, and W. Y. Ching, Phys. Rev. B **70**, 045103 (2004).
[59] P. Rulis, W. Y. Ching, and M. Kohyama, Acta Mater. **52**, 30009 (2004).
[60] W. Y. Ching, Lizhi Ouyang, Paul Rulis, and I. Tanaka, Phys. Status Solidi B **242**, R94 (2005).
[61] L. Ouyang and W. Y. Ching, J. Am. Ceram. Soc. **84**, 801 (2001).
[62] R. F. Egarton, *Electron Energy Loss Spectroscopy in the Electron Microscope* (Plenum, New York, 1996).
[63] Rik Brydson, *Electron Energy Loss Spectroscopy* (BIOS Scientific, Oxford, 2001).
[64] I. Tanaka, T. Mizoguchi, and T. Yamamoto, J. Am. Ceram. Soc. **88**, 2013 (2005).
[65] C. L. Bull, P. F. McMillan, J.-P. Itie, and A. Polian, Phys. Status Solidi A **201**, 909 (2005).